

Fracture Simulation Using an Elasto-Viscoplastic Virtual Internal Bond Model With Finite Elements

Ganesh Thiagarajan¹

e-mail: ganesh@umkc.edu
Department of Civil Engineering,
University of Missouri,
Kansas City, MO 64110

Yonggang Y. Huang

Department of Mechanical and Industrial
Engineering,
University of Illinois—Urbana-Champaign,
Urbana, IL 61801

K. Jimmy Hsia

Department of Theoretical and Applied
Mechanics,
University of Illinois—Urbana-Champaign,
Urbana, IL 61801

A virtual internal bond (VIB) model for isotropic materials has been recently proposed by Gao (Gao, H., 1997, "Elastic Waves in a Hyperelastic Solid Near its Plane Strain Equibiaxial Cohesive Limit," Philos. Mag. Lett. 76, pp. 307–314) and Gao and Klein (Gao, H., and Klein, P., 1998, "Numerical Simulation of Crack Growth in an Isotropic Solid With Randomized Internal Cohesive Bonds," J. Mech. Phys. Solids 46(2), pp. 187–218), in order to describe material deformation and fracture under both static and dynamic loading situations. This is made possible by incorporating a cohesive type law of interaction among particles at the atomistic level into a hyperelastic framework at the continuum level. The finite element implementation of the hyperelastic VIB model in an explicit integration framework has also been successfully described in an earlier work by the authors. This paper extends the isotropic hyperelastic VIB model to ductile materials by incorporating rate effects and hardening behavior of the material into a finite deformation framework. The hyperelastic VIB model is formulated in the intermediate configuration of the multiplicative decomposition of the deformation gradient framework. The results pertaining to the deformation, stress-strain behavior, loading rate effects, and the material hardening behavior are studied for a plate with a hole problem. Comparisons are also made with the corresponding hyperelastic VIB model behavior.

[DOI: 10.1115/1.1796451]

1 Introduction

It is well established that plastic deformation takes place in regions of high stress concentrations and that fracture at the crack tip is preceded by some degree of plastic deformation. To be more realistic the numerical simulations of crack initiation, propagation, and branching must, therefore, include the elastoplastic behavior of the material. Among the finite-element-based numerical models, which are becoming widely accepted, is the cohesive surface modeling of fracture. Many researchers, including Barenblatt [1], Dugdale [2], Willis [3], Xia and Shih [4], and Xu and Needleman [5], to mention a few, have worked on propagating and advancing this methodology. The fundamental basis of these models lies in defining discrete cohesive surfaces in which the traction and separation at the boundaries are described by nonlinear cohesive laws. These models do not require any separate fracture criterion. However, these surfaces, which lie in between element boundaries, must be defined a priori, and separate cohesive elements must be introduced in between boundaries of the regular finite elements.

In contrast to the approach described above, Gao [6,7] and Gao and Klein [8] proposed an approach called the Virtual Internal Bond (VIB) model, wherein the *constitutive model* directly incorporates a cohesive-type law. In the VIB approach, the continuum is treated as a random network of material points, interconnected by bonds, which obeys a cohesive law. The bonds are physically described by a bond energy $U(l)$, where l is the bond length, and its derivative with respect to the bond length $U'(l)$ is the cohesive

bond force. By describing this bond energy in a hyperelastic framework of finite deformation, the appropriate stress and strain measures, such as the Green-Lagrange strain tensor and the second Piola-Kirchhoff stress tensor, can be derived. The macroscopic description of the continuum is determined by the Cauchy-Born rule [9] of crystal elasticity, by equating the macroscopic strain energy function at the continuum level to the potential energy stored in the cohesive bonds at the microscale. The description of the bond length l in terms of the Green-Lagrange strain tensor provides the link between the two scales.

Klein and Gao [10] have described the application of the VIB model (based on the hyperelastic framework) to fracture initiation and propagation and have further studied the crack dynamics using this model. An implicit second-order integration scheme was used to simulate quasi-static and dynamic loading problems. Zhang et al. [11] implemented this model, using an implicit integration scheme, in a UMAT subroutine in ABAQUS [12]. The softening region of the cohesive models presents a major issue with the numerical implementation, using implicit integration schemes. Thiagarajan et al. [13] found that the explicit integration scheme is better suited for the finite element (FE) implementation of the VIB model. The model was implemented using the user subroutine VUMAT in ABAQUS. The influence of mesh shape and size, loading rate, and other related issues were studied for both quasi-static and dynamic impact loading cases [13]. The experimental verification and validation of the VIB model was studied for the case of dynamic fragmentation of brittle materials under impact loading by Thiagarajan et al. [14].

The work presented here stems from the previous work by the authors and is motivated by the observation that it is necessary to incorporate plastic deformation in regions of high stress concentrations. There are two basic approaches of incorporating plasticity into the VIB model. One is at the atomistic level by the consideration of individual dislocations (millions of them) and other microstructural features. This method is numerically daunting

¹Corresponding author.

Contributed by the Applied Mechanics Division of THE AMERICAN SOCIETY OF MECHANICAL ENGINEERS for publication in the ASME JOURNAL OF APPLIED MECHANICS. Manuscript received by the ASME Applied Mechanics Division, January 21, 2003; final revision, November 13, 2003. Editor: H. Gao. Discussion on the paper should be addressed to the Editor, Prof. Robert M. McMeeking, Journal of Applied Mechanics, Department of Mechanical and Environmental Engineering University of California—Santa Barbara, Santa Barbara, CA 93106-5070, and will be accepted until four months after final publication of the paper itself in the ASME JOURNAL OF APPLIED MECHANICS.

even with the current level of supercomputers. The second approach, which is adopted in this research, is to incorporate plasticity and/or viscoplasticity at the continuum level by using well-established plasticity and viscoplasticity models.

The incorporation of viscoplastic effects into the VIB model is done within the framework of the multiplicative decomposition of the deformation gradient $\mathbf{F} = \mathbf{F}^e \mathbf{F}^p$ proposed by Lee [15] and advanced by numerous authors. This description is outlined in a later section. The fracture simulation of a ductile material is studied by treating it as an elasto-viscoplastic solid. The elastic behavior is modeled as a hyperelastic VIB material and the plastic and/or viscoplastic response is defined in the so-called intermediate configuration. The model is studied using 6061 Al for which the viscoplastic material properties are available.

In this paper, Section 2 gives a brief description of the well-known finite deformation kinematic formulations in order to establish the scientific basis for the choice of the intermediate configuration. The elasto-viscoplastic constitutive formulation for the intermediate configuration is then described in Section 3. Section 4 describes the details of the explicit integration scheme details, and Section 5 describes the numerical finite element implementation, along with the results from various case studies. The conclusions are presented in Section 6.

2 General Kinematic Formulations

The choice of an appropriate strain and strain-rate measure is critical to the elasto-viscoplastic formulation of fracture for ductile materials using the VIB model. At the outset, various kinematic frameworks, both small strain and finite strain, are described below along with the possible situations to which they may be applied. The choice of the kinematic formulation that is best suited for the elastoplastic VIB model is then described in detail.

2.1 Small Strain Formulation. For problems where total strains are small, the additive decomposition of total strains (of the order of 0.001) are given as

$$\epsilon_{ij} = \epsilon_{ij}^e + \epsilon_{ij}^p \quad (1)$$

where the elastic strains are of the order of 0.001 (0.1%).

The uniaxial strains for ductile materials can reach the order of unity due to plastic flow, especially in metal-forming problems. In these cases the elastic strains (0.001) are very small compared to the total strains and can be neglected. The hydrostatic stress in such cases does not affect yielding, and only the deviatoric part of the stress causes yielding. The plastic flow can be expressed as a functional as shown below:

$$\dot{\epsilon}_{ij}^p = f_{ij}(\sigma, \dot{\sigma}) \quad (2)$$

As the elastic strains are neglected, the total strain rate can be expressed in terms of the derivatives of the velocity field as follows:

$$\dot{\epsilon}_{ij} = \dot{\epsilon}_{ij}^p \quad (3)$$

$$= \frac{1}{2} \left(\frac{\partial v_i}{\partial x_j} + \frac{\partial v_j}{\partial x_i} \right) \quad (4)$$

Final deformations are obtained by integrating Eq. (4) over time. This formulation is well known as the rigid plastic model and, although the total strains are finite, there is no need to use finite strain kinematics.

2.2 Finite Deformation Theory. The finite deformation framework is applicable to cases where the total strains are finite and the magnitude of elastic and plastic strains are comparable. Examples of these include cases where the inertia forces are high due to rapid loading as in explosive and impact loading. Elastic strains of the magnitude of 25% or more have been reported for explosive loading [16], which would necessitate a kinematic

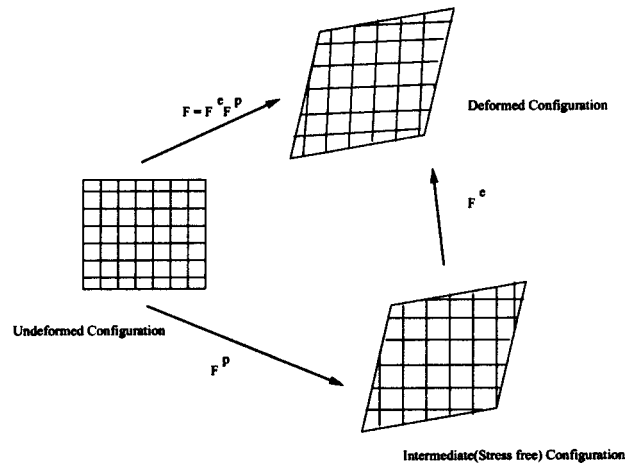


Fig. 1 Multiplicative decomposition of deformation gradient \mathbf{F} with its effect on shape and microstructure

framework where both elastic and plastic strains can be of finite magnitude. The kinematics involved in the formulation of finite elastic and inelastic deformations are based on the multiplicative decomposition of the deformation gradient and described in detail below.

2.3 Multiplicative Decomposition of Deformation Gradient. The *effective decoupling* of the elastic and plastic laws can be achieved by using the unstressed configuration for deformation changes. It is assumed that yielding is not affected by the hydrostatic Cauchy stresses and that the elastic constants are not affected by plastic deformations. In this paper, capital-letter subscripts are used for the initial configuration while lowercase subscripts are used for the deformed configuration.

A multiplicative framework for large deformation inelastic behavior is adopted [15–21] as follows:

$$\mathbf{F} = \mathbf{F}^e \cdot \mathbf{F}^p \quad \det \mathbf{F}^e, \det \mathbf{F}^p > 0 \quad (5)$$

$$F_{ij} = F_{ij}^e F_{ij}^p$$

where \mathbf{F} is the deformation gradient, \mathbf{F}^e is the elastic deformation gradient and \mathbf{F}^p is the plastic deformation gradient. As shown in Fig. 1, such a characterization allows for the definition of an imaginary intermediate relaxed (stress-free) configuration $\bar{\Omega}$. Ω_0 and Ω are the configurations at time $t = t_0$ and $t = t_{n+1}$, respectively. In this paper any quantity with an overbar ($\bar{\quad}$) refers to its value in the intermediate configuration. The intermediate configuration is commonly considered as a stress-free configuration obtained by elastically unloading the body from the current configuration. It can be physically considered to represent the total effect of dislocations without any lattice distortions (mapped by \mathbf{F}^p), while the lattice distortions and rotations transform the intermediate configuration to the current configuration (mapped by \mathbf{F}^e). The basic kinematic variables associated with the three configurations are now described.

2.3.1 Undeformed Configuration Ω_0 . The primary kinematic tensors associated with the undeformed configuration Ω_0 are the left Cauchy-Green deformation tensor \mathbf{C} and the Green-Lagrange strain tensor \mathbf{E} , which are expressed as follows:

$$\mathbf{C} = \mathbf{F}^T \cdot \mathbf{F} \quad \text{or} \quad C_{IJ} = F_{iI} F_{iJ} \quad (6)$$

$$\mathbf{E} = \frac{1}{2}(\mathbf{C} - \mathbf{G}) \quad \text{or} \quad E_{IJ} = \frac{1}{2}(C_{IJ} - G_{IJ}) \quad (7)$$

where \mathbf{G} is the metric tensor in the undeformed configuration. In the Cartesian coordinate system $G_{IJ} = \delta_{IJ}$ where δ_{IJ} is the Kronecker delta. Since the plastic deformation gradient maps the initial configuration to the intermediate configuration, the plastic

parts of the left Cauchy-Green deformation tensor \mathbf{C}^p and the Green-Lagrange strain tensor \mathbf{E}^p can be expressed as follows:

$$\mathbf{C}^p = \mathbf{F}^{pT} \cdot \mathbf{F}^p \quad \text{or} \quad C_{IJ}^p = F_{iI}^p F_{iJ}^p \quad (8)$$

$$\mathbf{E}^p = \frac{1}{2}(\mathbf{C}^p - \mathbf{G}) \quad \text{or} \quad E_{IJ}^p = \frac{1}{2}(C_{IJ}^p - G_{IJ}) \quad (9)$$

From the above definitions, the elastic component of the Green-Lagrange strain tensor is defined using the additive decomposition [22] as

$$\mathbf{E}^e = \mathbf{E} - \mathbf{E}^p \quad (10)$$

2.3.2 Intermediate Configuration $\bar{\Omega}$. The Green-Lagrange strain in the intermediate configuration $\bar{\mathbf{E}}$ can be defined as a push-forward transformation of \mathbf{E} using \mathbf{F}^p as follows:

$$\bar{\mathbf{E}} = \mathbf{F}^{pT} \mathbf{E} \mathbf{F}^p \quad (11)$$

$$= \bar{\mathbf{E}}^e + \bar{\mathbf{E}}^p \quad (12)$$

where

$$\bar{\mathbf{E}}^e = \frac{1}{2}(\mathbf{F}^{eT} \cdot \mathbf{F}^e - \mathbf{I}) \quad (13)$$

$$\bar{\mathbf{E}}^p = \frac{1}{2}(\mathbf{I} - \mathbf{F}^{pT} \cdot \mathbf{F}^p) \quad (14)$$

The deformation gradients \mathbf{F}^e , \mathbf{F}^p may not strictly be continuously differentiable mappings. They have sometimes been described as point matrix functions.

2.3.3 Current or Deformed Configuration Ω . The deformation gradients mapping the initial and the intermediate configurations into the current configuration (Fig. 1) are the total \mathbf{F} and elastic \mathbf{F}^e parts, respectively. Consequently, the primary strain tensors associated with the current configuration may be expressed as

$$\mathbf{b} = \mathbf{F} \cdot \mathbf{F}^T \quad \text{or} \quad b_{ij} = F_{iI} F_{jI} \quad (15)$$

$$\mathbf{e} = \frac{1}{2}(\mathbf{g} - \mathbf{b}^{-1}) \quad \text{or} \quad e_{ij} = \frac{1}{2}(g_{ij} - b_{ij}^{-1}) \quad (16)$$

$$\mathbf{b}^e = \mathbf{F}^e \cdot \mathbf{F}^{eT} \quad \text{or} \quad b_{ij}^e = F_{iI}^e F_{jI}^e \quad (17)$$

$$\mathbf{e}^e = \frac{1}{2}(\mathbf{g} - \mathbf{b}^{e-1}) \quad \text{or} \quad e_{ij}^e = \frac{1}{2}(g_{ij} - b_{ij}^{e-1}) \quad (18)$$

where \mathbf{b} and \mathbf{b}^e are the total and elastic right Cauchy-Green deformation tensors and \mathbf{e} and \mathbf{e}^e are the total and elastic Eulerian strain tensors, respectively. The additive decomposition of the Eulerian strain tensor leads to

$$\mathbf{e}^p = \mathbf{e} - \mathbf{e}^e \quad (19)$$

Following Marsden and Hughes [23], the tensors \mathbf{e} and \mathbf{e}^p may be referred to as the push forward, using \mathbf{F}^p , of the tensors \mathbf{E} and \mathbf{E}^p , respectively.

2.4 Rate of Deformation and Spin Tensors. The velocity gradient, rate of deformation, and spin tensors can be expressed in the current and intermediate configurations as described below.

2.4.1 Current Configuration. The velocity gradient of a particle defined in the current configuration is expressed as

$$\mathbf{L} = \frac{\partial \mathbf{v}}{\partial \mathbf{x}} = \dot{\mathbf{F}} \mathbf{F}^{-1} = \mathbf{D} + \mathbf{W} \quad (20)$$

$$\mathbf{D} = \text{symm}(\mathbf{L}) \quad (21)$$

$$\mathbf{W} = \text{skew}(\mathbf{L}) \quad (22)$$

where \mathbf{D} is the rate of deformation or velocity tensor representing the stretching part and \mathbf{W} is the spin rate tensor. By substituting the multiplicative decomposition of the deformation gradient in the above equation, one can derive the following expression:

$$\mathbf{L} = (\dot{\mathbf{F}}^e \cdot \mathbf{F}^{e-1}) + (\mathbf{F}^e \cdot \dot{\mathbf{F}}^p \cdot \mathbf{F}^{p-1} \cdot \mathbf{F}^e) = (\mathbf{L}^e) + (\mathbf{L}^p) \quad (23)$$

$$= (\mathbf{D}^e + \mathbf{W}^e) + (\mathbf{D}^p + \mathbf{W}^p) \quad (24)$$

where \mathbf{L}^e and \mathbf{L}^p are the definitions of the elastic and plastic velocity gradient tensors and \mathbf{D}^e , \mathbf{D}^p , \mathbf{W}^e , \mathbf{W}^p are the elastic and plastic parts of the stretching-rate and spin-rate tensors, respectively. In theory it can be assumed that not only the symmetric part \mathbf{D}^p but also the skew symmetric part \mathbf{W}^p is governed by constitutive equations. For rate-dependent materials [24], these constitutive equations can be expressed as

$$\mathbf{D}^p = \mathbf{F}^e \mathbf{D}^p(F^{eT} \mathbf{F}^e, \alpha) \mathbf{F}^{e-1} \quad (25)$$

$$\mathbf{W}^p = \mathbf{F}^e \mathbf{W}^p(F^{eT} \mathbf{F}^e, \alpha) \mathbf{F}^{e-1} \quad (26)$$

where α is a set of parameters that describe structural changes caused by lattice defects. Wang's [25] representation theorem yields $\mathbf{W}^p = 0$, thereby ignoring the effect of the plastic spin-rate tensor.

2.4.2 Intermediate Configuration. Since the velocity gradient has a covariant-contravariant character, using an appropriate pull back from the current configuration, the expression for its representation in the intermediate configuration results in

$$\bar{\mathbf{L}} = \mathbf{F}^{e-1} \mathbf{L} \mathbf{F}^e \quad (27)$$

$$= \mathbf{F}^{e-1} \dot{\mathbf{F}}^e + \dot{\mathbf{F}}^p \mathbf{F}^{p-1} = \bar{\mathbf{L}}^e + \bar{\mathbf{L}}^p \quad (28)$$

where $\bar{\mathbf{L}}^e$ and $\bar{\mathbf{L}}^p$ are the elastic and plastic velocity gradient tensors. The rate of deformation tensors in the intermediate configuration can be expressed as

$$\bar{\mathbf{D}} = \text{symm}(\bar{\mathbf{L}}) = \frac{1}{2}(\bar{\mathbf{C}}^e \bar{\mathbf{L}} + \bar{\mathbf{L}}^T \bar{\mathbf{C}}^e) = \mathbf{F}^{eT} \mathbf{D} \mathbf{F}^e \quad (29)$$

$$\bar{\mathbf{D}}^e = \text{symm}(\bar{\mathbf{L}}^e) = \frac{1}{2}(\bar{\mathbf{C}}^e \bar{\mathbf{L}}^e + \bar{\mathbf{L}}^{eT} \bar{\mathbf{C}}^e) = \mathbf{F}^{eT} \mathbf{D}^e \mathbf{F}^e \quad (30)$$

$$\bar{\mathbf{D}}^p = \text{symm}(\bar{\mathbf{L}}^p) = \frac{1}{2}(\bar{\mathbf{C}}^p \bar{\mathbf{L}}^p + \bar{\mathbf{L}}^{pT} \bar{\mathbf{C}}^p) = \mathbf{F}^{eT} \mathbf{D}^p \mathbf{F}^e \quad (31)$$

3 Elastic-Viscoplastic Constitutive Assumptions

In the approach proposed in this paper, the hyperelastic-viscoplastic response of the VIB model is based on the following assumptions:

1. The intermediate configuration is assumed to be the basis for the definition of the plastic variables. As the intermediate configuration is considered to be a fixed configuration associated only with lattice deformations, the elastic bonds between the particles are not affected. This configuration is obtained by elastically unloading the material from the current configuration. The original hyperelastic VIB model is hence set up in the intermediate configuration.
2. The *flow rule* is specified in terms of the plastic part of the velocity gradient $\bar{\mathbf{L}}^p$. This is assumed to be a function of the Piola-Kirchhoff stress and other internal variables.
3. The solid is considered to be isotropic in the intermediate configuration leading to the assumption that the plastic part of the spin tensor is zero ($\bar{\mathbf{W}}^p = 0$).
4. A unified viscoplastic model is assumed, where inelastic strains include plastic and creep strains, by specifying a single set of flow rules and evolutionary equations.
5. The stress rate is assumed to have no effect on the evolutionary equations, i.e., instantaneous plasticity is neglected.
6. Plastic deformations are assumed to be incompressible or $\det(\mathbf{F}^p) = 1$.

3.1 Intermediate Configuration Formulation. Based on the hypothesis of formulating the hyperelastic part of the elasto-viscoplastic VIB formulation in the intermediate configuration, the final kinematic quantities used in this formulation are summarized as follows:

$$\begin{aligned}
\mathbf{F} &= \mathbf{F}^e \cdot \mathbf{F}^p \\
\mathbf{L} &= \dot{\mathbf{F}}\mathbf{F}^{-1} = \mathbf{D} + \mathbf{W} \\
\mathbf{L} &= (\dot{\mathbf{F}}^e \cdot \mathbf{F}^{e-1}) + (\mathbf{F}^e \cdot \dot{\mathbf{F}}^p \cdot \mathbf{F}^{p-1} \cdot \mathbf{F}^{e-1}) = (\mathbf{L}^e) + (\mathbf{F}^e \bar{\mathbf{L}}^p \mathbf{F}^{e-1}) \\
&= \mathbf{L}^e + \mathbf{L}^p = (\mathbf{D}^e + \mathbf{W}^e) + (\mathbf{D}^p + \mathbf{W}^p) \\
\bar{\mathbf{L}} &= \mathbf{F}^{e-1} \mathbf{L} \mathbf{F}^e = \mathbf{F}^{e-1} \dot{\mathbf{F}}^e + \dot{\mathbf{F}}^p \mathbf{F}^{p-1} = \bar{\mathbf{L}}^e + \bar{\mathbf{L}}^p \\
\bar{\mathbf{L}}^e &= \mathbf{F}^{e-1} \cdot \dot{\mathbf{F}}^e \\
\bar{\mathbf{L}}^p &= \dot{\mathbf{F}}^p \cdot \mathbf{F}^{p-1}
\end{aligned}$$

3.2 Hyperelastic Constitutive Equations. The original Virtual Internal Bond (VIB) elastic model has been formulated in the reference configuration [6,7,10]. The Cauchy-Born rule of crystal elasticity is used to derive the overall constitutive equations by equating the internal strain energy of the bonds to the potential energy stored in the continuum due to external forces. The initial and the deformed configurations are defined using the Lagrangian coordinates $\mathbf{X} = X_I$ and the Eulerian coordinates $\mathbf{x} = \mathbf{x}(\mathbf{X}, t) = x_i(X_I, t)$, respectively. The deformation gradient \mathbf{F} and the Green-Lagrange strain tensor \mathbf{E} are used in the basic elastic description.

Consider an arbitrary microstructural bond at an angle θ and ϕ , where θ is the angle between the bond and the vertical positive z -axis, and ϕ is the angle in the horizontal plane with respect to the positive x -axis (in polar coordinates), respectively. The unit vector along this direction is given as $\xi = (\sin \theta \cos \phi, \sin \theta \sin \phi, \cos \theta)$ with respect to the undeformed configuration. The stretch of this bond can be given as

$$l = l_o \sqrt{1 + 2\xi_I E_{IJ} \xi_J} \quad (32)$$

The macroscopic strain energy density function is derived using the Cauchy-Born rule [9,26] as

$$\psi(E_{IJ}) = \langle U(l) \rangle \quad (33)$$

where $\langle \dots \rangle$ represents the weighted average with respect to the bond density function D_d . $U(l)$ is the potential energy function between each bond. Assuming that all bonds have the same initial length l_o , for the general case this is given as,

$$\langle \dots \rangle = \int_0^{2\pi} \int_0^\pi \dots D_d(\theta, \phi) \sin \theta d\theta d\phi \quad (34)$$

The term $D_d(\theta, \phi) \sin(\theta) d\theta d\phi$ represents the number of bonds per unit volume between the bond angles $(\theta, \theta + d\theta)$ and $(\phi, \phi + d\phi)$. For isotropic solids the bond density function is taken as a constant D_o . Hence the macroscopic strain energy density function can be now given as

$$\psi(E_{IJ}) = D_o \int_0^{2\pi} \int_0^\pi U(l) \sin \theta d\theta d\phi \quad (35)$$

For a two-dimensional isotropic solid subjected to plane stress, the bond density function can be expressed as $D_d \delta[\theta - (\pi/2)]$ and the strain energy density function becomes

$$\psi = D_o \int_0^{2\pi} U(l) d\phi \quad (36)$$

From the strain energy density function ψ , the symmetric second Piola-Kirchoff stress S_{IJ} and the elastic modulus A_{IJKL} can be derived as follows:

$$\mathbf{S} = \frac{\partial \psi}{\partial \mathbf{E}} \quad \text{or} \quad S_{IJ} = \frac{\partial \psi}{\partial E_{IJ}} \quad (37)$$

$$A_{IJKL} = \frac{\partial^2 \psi}{\partial E_{IJ} \partial E_{KL}} \quad (38)$$

The modulus derived from this potential satisfies the major and minor symmetries, $A_{IJKL} = A_{JIKL} = A_{IJLK} = A_{KLIJ}$, as well as the Cauchy symmetry, $A_{IJKL} = A_{IKJL}$. This results in only one isotropic elastic constant being needed. This is due to the fact that the Cauchy symmetry is satisfied by the fourth-order isotropic elasticity tensor only for the case of $\lambda = \mu$, where λ and μ are the two Lamé constants.

3.2.1 Adaptation to the Proposed Model. In the proposed model, since the intermediate configuration is considered to be a fixed configuration associated only with lattice deformations, the elastic bonds between the particles are not affected in this configuration. Hence, the elastic VIB response in the intermediate configuration can now be expressed as

$$\bar{\mathbf{S}} = \frac{\partial \bar{\psi}(\bar{\mathbf{E}}^e)}{\partial \bar{\mathbf{E}}^e} \quad \text{or} \quad \bar{S}_{IJ} = \frac{\partial \bar{\psi}}{\partial \bar{E}_{IJ}^e} \quad (39)$$

where $\bar{\mathbf{S}}$ is the equivalent of second Piola-Kirchoff stress in the intermediate configuration.

3.3 Viscoplastic Response Formulation. The intermediate configuration can be uniquely described by the plastic part of the deformation gradient \mathbf{F}^p , and the evolution equations can be set up to describe it using an appropriate flow rule. The two internal variables, namely, the backstress $\bar{\alpha}$ and the effective accumulated plastic strain $\bar{\epsilon}^p = \int_0^t \dot{\bar{\epsilon}}^p dt$, and the evolution equations in the rate-dependent form are described here. The constitutive equations formulated here is based on the elasto-viscoplastic response of a material following the J_2 flow theory.

The expressions for the deviatoric form of the second Piola-Kirchoff stress and the backstress (in the intermediate configuration) can be expressed as follows:

$$\bar{\mathbf{S}}^d = \bar{\mathbf{S}} - \frac{1}{3}(\bar{\mathbf{S}} : \bar{\mathbf{C}}^e) \bar{\mathbf{C}}^{e-1} \quad (40)$$

$$\bar{\alpha}^d = \bar{\alpha} - \frac{1}{3}(\bar{\alpha} : \bar{\mathbf{C}}^e) \bar{\mathbf{C}}^{e-1} \quad (41)$$

and the hydrostatic pressure p is given by the equation $3Jp = \bar{\mathbf{S}} : \bar{\mathbf{C}}^e$, where J is the determinant of the deformation gradient.

Yield function. The yield function in the intermediate configuration is described as

$$\bar{\Phi}(\bar{\mathbf{S}}, \bar{\alpha}, \bar{\epsilon}^p) = 0 \quad (42)$$

For the J_2 flow theory the yield function takes the form

$$\bar{\Phi} = \bar{\sigma}_{eq}^2 - \kappa^2 = 0 \quad (43)$$

where the equivalent stress in the intermediate configuration is given as

$$\bar{\sigma}_{eq}^2 = \frac{3}{2}(\bar{\mathbf{S}}^d - \bar{\alpha}^d) : (\bar{\mathbf{S}}^d - \bar{\alpha}^d) \bar{\mathbf{C}}^e \bar{\mathbf{C}}^e \quad (44)$$

Flow rule. The flow rule is expressed as the evolution of the plastic part of the velocity gradient as follows:

$$\bar{\mathbf{L}}^p = \dot{\mathbf{F}}^p \mathbf{F}^{p-1} = \bar{\mathbf{D}}^p + \bar{\mathbf{W}}^p \quad (45)$$

$$= \lambda \bar{\mathbf{n}}(\bar{\mathbf{S}}, \bar{\alpha}, \bar{\epsilon}^p) \quad (46)$$

where $\bar{\mathbf{n}}$ is a second-order tensor representing the direction of plastic flow. Adopting the associated flow rule, this direction is normal to the yield surface. Using Eq. (44), the plastic flow direction can be expressed as

$$\bar{\mathbf{n}} = \frac{3}{2\bar{\sigma}_{eq}} (\bar{\mathbf{S}}^d - \bar{\alpha}^d) \bar{\mathbf{C}}^e \bar{\mathbf{C}}^e \quad (47)$$

and the evolution of the effective plastic strain rate is then given as follows:

$$\dot{\bar{\epsilon}}^p = \dot{\lambda} = \frac{\bar{\Phi}(\bar{\mathbf{S}}, \bar{\alpha}, \bar{\epsilon}^p)}{\eta} \quad (48)$$

where η is the viscosity parameter of the material (also referred to as the fluidity coefficient). The plastic part of the spin tensor ($\bar{\mathbf{W}}^p=0$) is not considered. These considerations result in a reduced form of the flow rule shown below

$$\bar{\mathbf{D}}^p = \lambda \text{symm}(\bar{\mathbf{n}}) \quad (49)$$

Hardening rule. The evolution of backstress is given by a kinematic hardening rule as follows:

$$\dot{\bar{\alpha}} = \lambda \bar{\mathbf{h}}(\bar{\mathbf{S}}, \bar{\alpha}, \bar{\epsilon}^p) \quad (50)$$

where $\bar{\mathbf{h}}$ is the hardening function.

4 Integration Procedure

The details and issues involved with the numerical implementation of the model proposed above are described in this section. The steps outlined here are presented in a format that is suitable for implementation using the ABAQUS subroutine VUMAT. In the material model, which involves the integration of the constitutive equations, the following data are given as input from ABAQUS: \mathbf{F}_t , \mathbf{F}_{t+1} , Δt , which represent the deformation gradients at the previous and current time step and the increment of time, respectively. The elastic and plastic deformation gradients at time t denoted by \mathbf{F}_t^e and \mathbf{F}_t^p , respectively, and the effective plastic strain $\bar{\epsilon}^p$ are designated and computed as state variables within the material model subroutine. The Cauchy stress σ_t from the previous time step is also returned back by ABAQUS for use if needed. The Cauchy stress tensor at time $(t+1)$, σ_{t+1} , along with the updated values of \mathbf{F}_{t+1}^p , \mathbf{F}_{t+1}^e , $\bar{\epsilon}^p$ are calculated and stored at the end of the current time step.

4.1 Numerical Integration Procedure

Step 1. The flow rule is integrated using an *implicit exponential approximation*, keeping the flow direction and the plastic modulus fixed during the current time step, as follows:

$$*\mathbf{F}_{n+1}^p = \exp[\Delta \bar{\epsilon}_{n+1}^p \bar{\mathbf{n}}_n] \bar{\mathbf{F}}_n^p \quad (51)$$

The tensor exponential function in Eq. (51) can be represented by a series representation as shown below

$$\exp[\mathbf{A}] = \sum_{n=0}^{\infty} \frac{1}{n!} [\mathbf{A}]^n \quad (52)$$

Considering the first two terms of the expansion of Eq. (51) and using the series representation, the flow rule and the resulting trial plastic deformation gradient can be expressed as given below

$$*\mathbf{F}_{t+1}^p = [\mathbf{I} + \Delta \bar{\epsilon}_{t+1}^p \bar{\mathbf{n}}_t] \bar{\mathbf{F}}_t^p \quad (53)$$

where \mathbf{I} is the second order identity tensor.

Step 2. The *trial* elastic deformation gradient for the current step is computed as follows:

$$*\mathbf{F}_{t+1}^e = (\mathbf{F})_{t+1} \mathbf{F}_{t+1}^{p-1} \quad (54)$$

$$*F_{ij}^e = (F_{iK})_{t+1} (F_{kJ})_{t+1}^{p-1}$$

Step 3. The Green strain can then be computed as shown below

$$*\bar{\mathbf{E}}_{t+1}^e = \frac{1}{2} [*\mathbf{F}_{t+1}^{eT} *\mathbf{F}_{t+1}^e - \mathbf{I}] \quad (55)$$

Step 4. The *trial elastic* second Piola-Kirchoff stress (based on the computation of new bond lengths in the intermediate configuration and assuming that the hyperelastic potential is based on the elastic stretch only) is calculated using the following equation:

$$*\bar{\mathbf{S}}_{t+1} = \frac{\partial \bar{\psi}(*\bar{\mathbf{E}}_{t+1}^e)}{\partial *\bar{\mathbf{E}}_{t+1}^e} \quad (56)$$

$$*(\bar{S}_{IJ})_{t+1} = \frac{\partial \bar{\psi}}{\partial *\bar{E}_{IJ}^e}$$

Step 5. The trial backstress is then updated by the following equation:

$$*\bar{\alpha}_{t+1} = \bar{\alpha}_t + \Delta \bar{\epsilon}_{t+1}^p \mathbf{h}_n \quad (57)$$

Step 6. The equivalent plastic strain, actual equivalent stress, and internal scalar or tensor variables can then be solved using a Newton iteration. The equivalent plastic strain increment can be expanded as

$$\Delta \bar{\epsilon}_{t+1}^p = \Delta t \dot{\bar{\epsilon}}^p (*\bar{\mathbf{S}}_{t+1}, *\mathbf{F}_{t+1}^p, \Delta \bar{\epsilon}_{t+1}^p, \bar{\alpha}_{t+1}) \quad (58)$$

The equivalent plastic strain increment in Eq. (58) is solved from the steps described using the Newton-Raphson technique with an initial guess of zero. This value is incremented until Eq. (58) is satisfied to some acceptable tolerance. The algorithm described above is a combination of both explicit and implicit steps.

5 Numerical Implementation

The numerical implementation of the finite deformation viscoplastic VIB model, described in the above sections, has been tested on a plate with a center-hole (PWH) problem. A number of issues, such as crack initiation and propagation, stress-strain behavior of cracked elements, development of plastic strain in elements, time of solution, etc., have been studied. The results are presented in this paper. Simulations have also been run using the elastic VIB model described in [13,14] and compared with the viscoplastic model.

In the simulations, 6061 Al has been used with a Young's Modulus of 70 GPa and a Poisson ratio of 0.3. The material has an initial yield stress $\bar{\sigma}_0 = 135$ MPa. The size of the quarter plate is taken as 100×100 mm. The plastic flow for this material is described by a power law given by the following equation [27]:

$$\bar{\sigma} = a + b(c + \kappa)^d \quad (59)$$

where the material constants with $a = 25$ MPa, $b = 466$ MPa, $c = 0.003$, and the exponent $d = 0.293$. κ is the equivalent plastic strain. The fluidity coefficient η used in the effective plastic strain-rate equation (48) is 5000 MPa/s.

5.1 Plate With Hole Problem: Unidirectional Displacement Loading. The loading cases studied for this problem are shown in Fig. 2. The displacement at the top edge of the plate is increased linearly in all cases with the rate being controlled by the

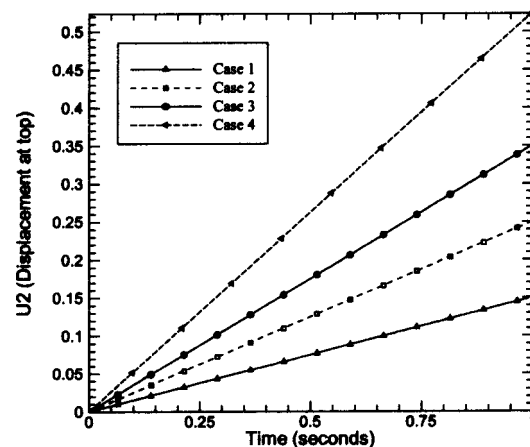


Fig. 2 Loading cases studied for plate with hole

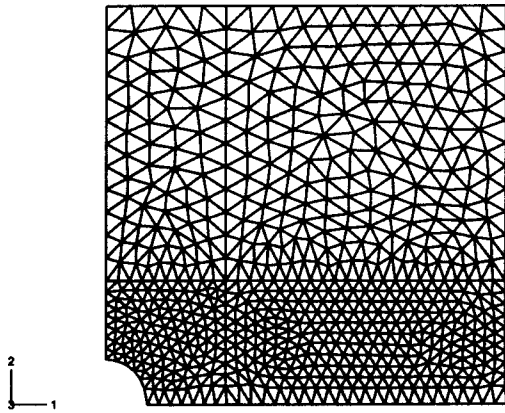


Fig. 3 Final deformation for elastic VIB model (case 2)

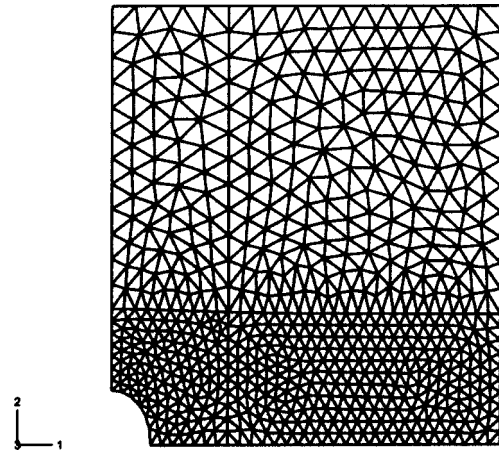


Fig. 5 Final deformation for viscoplastic VIB model (case 3)

final displacement value. All displacements are given during a real time of 1 s. The four cases correspond to a maximum displacement (U_2) of 1.5, 2.5, 3.5, and 5.3 mm, respectively, of the top of the plate. Both the elastic VIB model and the elasto-viscoplastic VIB (EPVIB) model have been run on the same data set.

For case 1 ($U_2=1.5$ mm), no cracking was observed for both the models, and hence, the results are not shown graphically. Figures 3 and 4 show the deformation of the VIB and EPVIB models, respectively, for case 2 ($U_2=2.5$ mm). A fully cracked band at the bottom edge can be seen for the elastic case (Fig. 3) while no cracking is observed in the EPVIB case (Fig. 4). For subsequent load cases the elastic deformation pattern is not shown as the bottom edge is fully cracked in all cases and is similar to that shown in Fig. 3. Figure 5 shows the final deformation for loading case 3 ($U_2=3.5$ mm) with the EPVIB model. A small crack is seen to develop at the bottom left edge with two or three elements showing cracks. Figure 6 shows the deformation pattern for case 4 ($U_2=5.3$ mm) at time 0.7 s from which it can be seen that the crack tip located at about one-third of the base length from the edge of the hole.

Figure 7 shows the stress distribution along the path defined by the bottom edge of the plate (for loading case 4), showing the stress values with increasing time, after cracking. The peak stress is indicative of the current location of the crack tip, shifts to the right. After the crack has fully propagated throughout the bottom edge, the stresses in these elements drop significantly, as shown in Fig. 7 at time steps $t=0.9$ s. Figure 8 shows the plot of crack tip location with time up to the time of 0.875 s. It was observed earlier that at 0.9 s the crack suddenly propagates throughout the bottom of the plate.

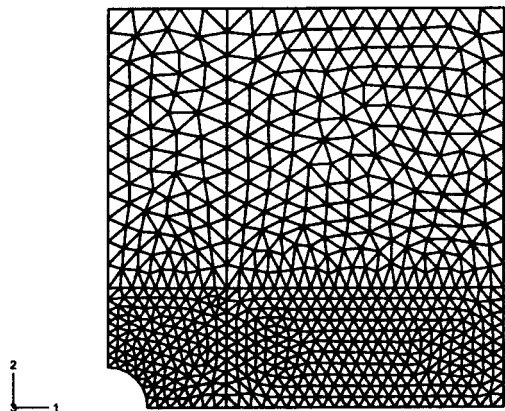


Fig. 4 Final deformation for viscoplastic VIB model (case 2)

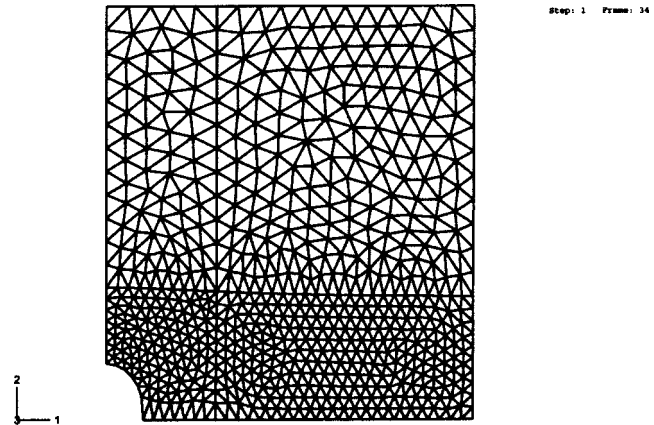


Fig. 6 Final deformation for viscoplastic VIB model ($t=0.7$ s) (case 4)

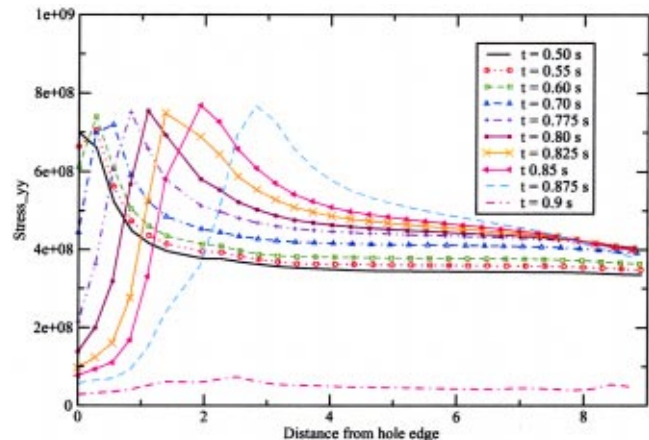


Fig. 7 Stress (σ_{yy}) distribution along bottom edge of plate (after cracking)

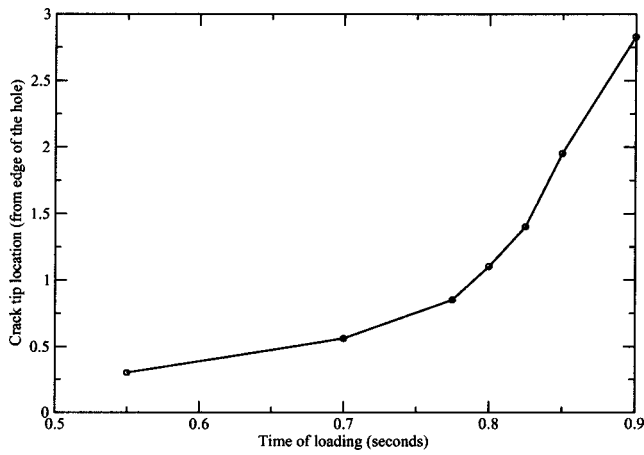


Fig. 8 Plot of crack tip location with time

Fig. 9. The peak of the viscoplastic response is higher than the elastic response and is due to the incorporation of the hardening behavior exhibited by the material.

Figure 10 shows the plot of the equivalent Mises stress with the equivalent plastic strain, for the left-bottom corner element. The intent of this figure is to study the effect of rate of loading on the development of plastic strains. After yielding, for loading cases 1 and 2 equivalent plastic strains are allowed to develop as the

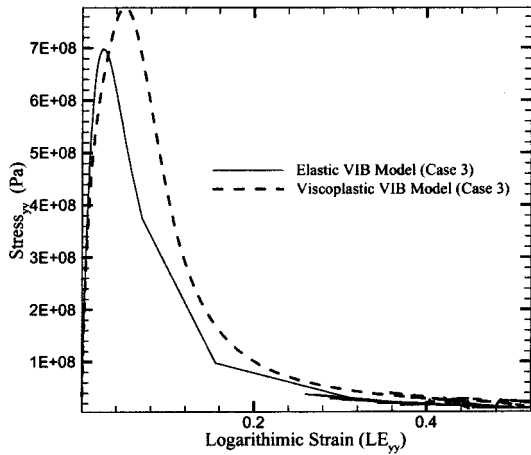


Fig. 9 Stress-strain curve for left-bottom corner element (case 3)

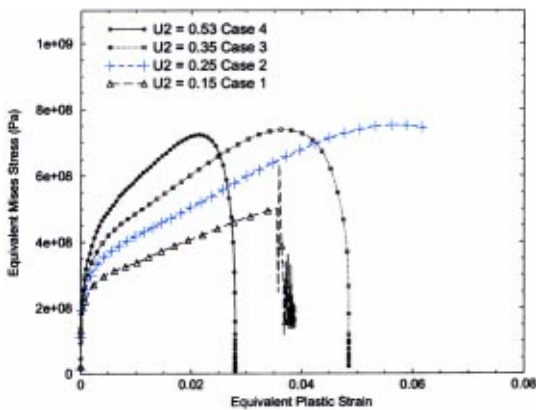


Fig. 10 Mises stress-equivalent plastic strain plots for left-corner element

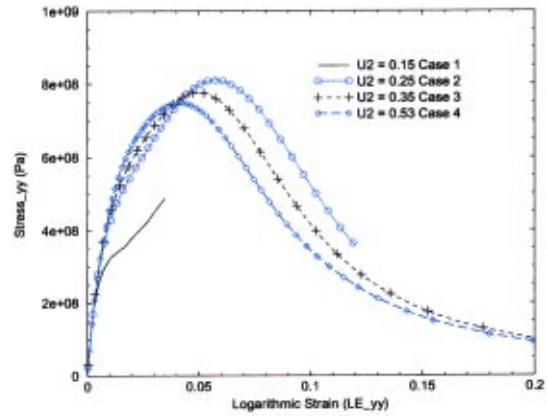


Fig. 11 Comparison of viscoplastic model stress-strain curves

loading rates are fairly low. In cases 3 and 4, which are simulated at a higher loading rate, the equivalent Mises stresses developed are higher while the plastic strains developed are lower compared to loading cases 1 and 2. The sudden drop in the stress in loading cases 3 and 4 are a consequence of the cracking of the element.

Figure 11 shows the comparative response for various loading cases for the viscoplastic model for the left corner element. The elastic response, which is not shown here, for these loading rates was observed to be identical for all the loading cases up to the point of maximum stress. The deviations in the softening region are due to numerical issues. For the viscoplastic model (Fig. 11), as the loading rate increases the peak stress and peak strain sustained appears to decrease. This might indicate that, for higher loading rates, the tendency to fracture is higher as plastic strains do not have time to develop.

The influence of material parameters (such as yield strength, fluidity coefficient, and hardening coefficient) on fracture properties, particularly, the cohesive strength and strain at the cohesive strength, have been studied. Figures 12–14 show the stress-strain behavior of the left-bottom corner element of the plate for different values of yield strength, fluidity coefficient, and hardness coefficient, respectively. The loading rate was kept the same in all these simulations.

From Fig. 12, which shows the variation for different yield strength values with the hardness and fluidity coefficient remaining the same, it can be seen that cohesive strength is not affected very much by the change in yield strength. The cohesive strain for

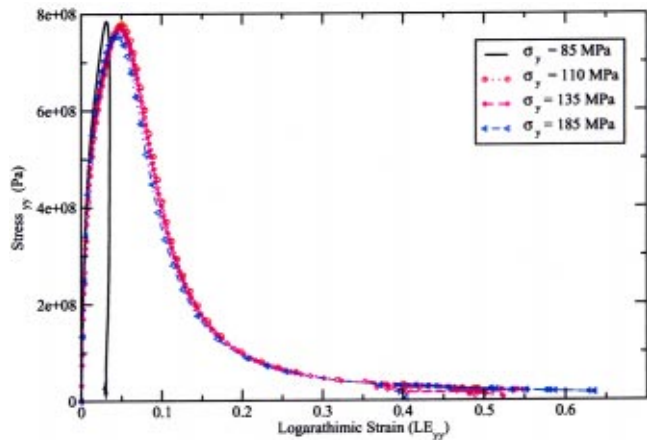


Fig. 12 Comparison of stress strain curves for different yield strengths

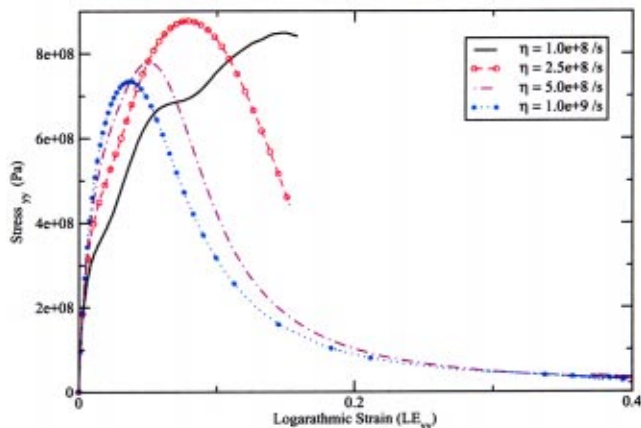


Fig. 13 Comparison of stress strain curves for different fluidity coefficients

yield strength of an 85 MPa value is lower compared to the yield strength values of 110, 135, and 185 MPa, which have very similar cohesive strain values.

Figure 13 shows the variation of the stress-strain behavior for the left-bottom corner element with varying fluidity coefficient values. It can be clearly seen that as the fluidity coefficient increases, both the cohesive stress and the cohesive strain values decrease, indicating that there is a faster tendency to fracture. Figure 14, which shows the variation of the stress strain curves for different values of hardness coefficient κ , indicates that the hardness coefficient has negligible influence on fracture.

5.2 Plate With Hole Problem: Biaxial Loading. The PWH problem was repeated with a biaxial load. The magnitude of loading was similar to that of loading case 3 of the uniaxial case with the loading now applied in two directions. A uniform velocity in both the x and y directions was applied over one second. Figures 15 and 16 show the final cracked configuration for the elastic and viscoplastic cases, respectively. A crack emanating from approximately the center of the quarter circular arc and propagating at a 45-deg angle can be clearly seen. The elastic model cracks earlier than the viscoplastic model case and also propagates much further. From Fig. 17, which shows a comparison of the stress and the logarithmic strain for the biaxial and uniaxial cases, it can be seen that the cohesive stress for biaxial stretching is lower and occurs at a lower strain value when compared to the uniaxial case. This observation is consistent with the theoretical derivation shown in

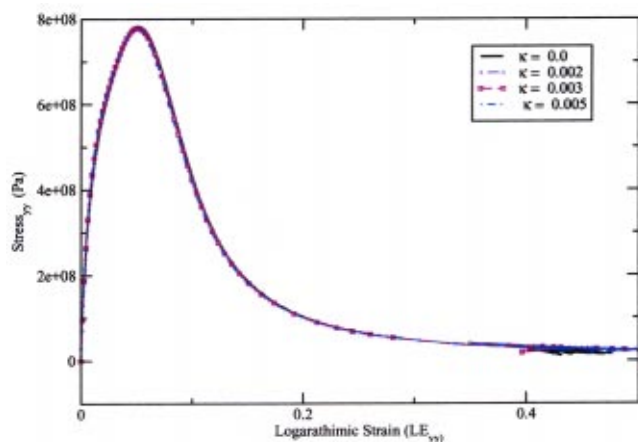


Fig. 14 Comparison of stress strain curves for different hardness coefficients

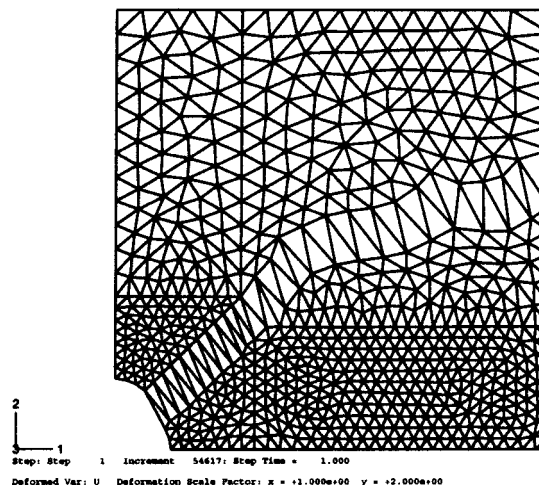


Fig. 15 Cracked pattern for biaxial load case with elastic VIB model

(Fig. 6 of Gao and Klein [8]). Figure 18 shows the comparison of the Mises stress and the equivalent plastic strain plots. Since the cohesive stress for the biaxial case is lower, the overall development of the equivalent plastic strain is also lower.

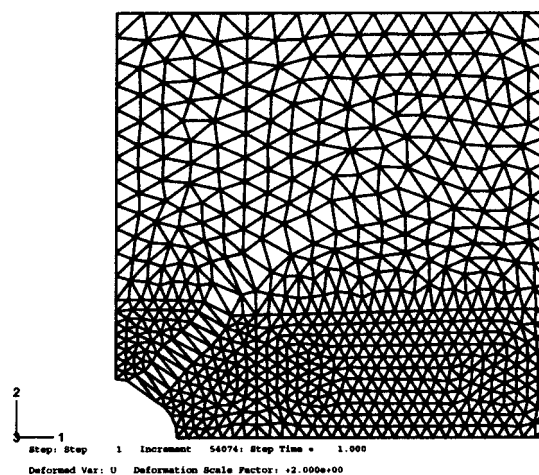


Fig. 16 Cracked pattern for biaxial load case with viscoplastic VIB model

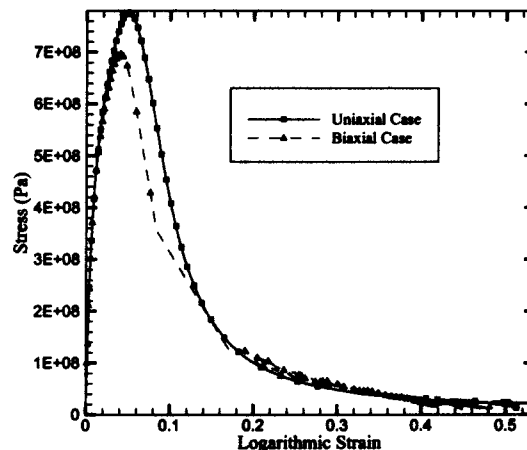


Fig. 17 Comparison of stress and logarithmic strains for the elastic and viscoplastic models

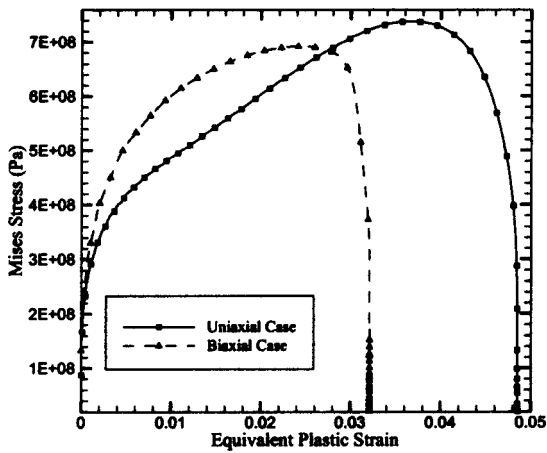


Fig. 18 Comparison of equivalent plastic strains for uniaxial and biaxial loading cases

6 Conclusions

In this paper an effective and robust finite element implementation of a hyperelasto-viscoplastic virtual internal bond model has been presented to simulate crack initiation, propagation, and branching in ductile materials. The following conclusions can be drawn from the paper.

1. Since the model is set up in an explicit integration framework, the softening region does not pose any difficulties due to possible negative eigenvalues or singularities in the stiffness matrix.
2. The effect of the plastic zone ahead of the crack tip is clearly demonstrated in the deformation patterns exhibited by the elastic and the viscoplastic VIB model.
3. The effect of strain hardening is also seen in the form of increased cohesive stress limits in the viscoplastic case.
4. The effect of loading rate on the development of plastic strains and crack formation has also been shown. It is seen that as loading rate increases, while the Mises stresses are higher, the plastic strains developed are lower. The material tends to crack earlier as the loading rate increases.
5. In parametric studies in which the effect of yield strength, fluidity coefficient, and hardness coefficient on fracture was studied, it was found that the yield strength and the hardness coefficient did not have a significant influence on the cohesive stress. However, an increase in the fluidity coefficient resulted in a decrease in the cohesive stress as well as the strain value.
6. The cohesive stress for biaxial stretching is lower and occurs at a lower strain value when compared to the uniaxial case. This observation is consistent with the theoretical derivation shown in (Fig. 6 of Gao and Klein [8]).

Acknowledgments

G.T. acknowledges the partial support by National Computational Science Alliance (Grant No. OND), and utilized the SGI Origin 2000 and the University of Missouri Research Board Grant (UMRB). Y.H. acknowledges the support from NSF (Grant No.

9983779), ONR (Grant No. N00014-01-1-0205, program officer Dr. Y. D. S. Rajapakse), and ASCI Center for Simulation of Advanced Rockets at the University of Illinois, supported by U.S. Department of Energy through the University of California under Subcontract No. B523819. K.J.H. also acknowledges partial financial support from NSF.

References

- [1] Barenblatt, G. I., 1959, "The Formation of Equilibrium Cracks During Brittle Fracture: General Ideas and Hypotheses, Axially Symmetric Cracks," *J. Appl. Math. Mech.*, **23**, pp. 622–636.
- [2] Dugdale, D. S., 1960, "Yielding of Steel Sheets Containing Slits," *J. Mech. Phys. Solids*, **8**, pp. 100–104.
- [3] Willis, J. R., 1967, "A Comparison of the Fracture Criteria of Griffith and Barenblatt," *J. Mech. Phys. Solids*, **15**, pp. 151–162.
- [4] Xia, L., and Shih, F. C., 1995, "Ductile Crack Growth-I. A Numerical Study Using Computational Cells With Microstructurally Based Length Scales," *J. Mech. Phys. Solids*, **43**(2), pp. 233–259.
- [5] Xu, X. P., and Needleman, A., 1994, "Numerical Simulation of Fast Crack Growth in Brittle Solids," *J. Mech. Phys. Solids*, **42**(9), pp. 1397–1434.
- [6] Gao, H., 1997, "Elastic Waves in a Hyperelastic Solid Near its Plane Strain Equibiaxial Cohesive Limit," *Philos. Mag. Lett.*, **76**, pp. 307–314.
- [7] Gao, H. A., 1996, "Theory of Local Limiting Speed in Dynamic Fracture," *J. Mech. Phys. Solids*, **44**, pp. 1453–1474.
- [8] Gao, H., and Klein, P., 1998, "Numerical Simulation of Crack Growth in an Isotropic Solid With Randomized Internal Cohesive Bonds," *J. Mech. Phys. Solids*, **46**(2), pp. 187–218.
- [9] Tadmor, E. B., Ortiz, M., and Phillips, R., 1996, "Quasicontinuum Analysis of Defects in Solids," *Philos. Mag. A*, **73**, pp. 1529–1563.
- [10] Klein, P., and Gao, H., 1998, "Crack Nucleation and Growth as Strain Localization in a Virtual Internal Bond Continuum," *Eng. Fract. Mech.*, **61**, pp. 21–48.
- [11] Zhang, P., Klein, P., Huang, Y., Gao, H., and Wu, P. D., 2002, "Numerical Simulation of Cohesive Fracture by the Virtual Internal Bond Method," *Comput. Model. Eng. Sci.*, **3**, pp. 263–278.
- [12] *ABAQUS/Explicit Users Manual*, HKS Inc.
- [13] Thiagarajan, G., Hsia, K. J., and Huang, Y. Y., 2004, "Finite Element Implementation of Virtual Internal Bond Model for Simulating Crack Behavior," *Eng. Fract. Mech.*, **71**, pp. 401–423.
- [14] Thiagarajan, G., Hsia, K. J., and Huang, Y. Y., 2002, "Experimental Verification and Validation of Virtual Internal Bond Parameters for Simulating Dynamic Crack Behavior," *Proc. 39th Annual Technical Meeting of Society of Engineering Science-SES 2002*.
- [15] Lee, E. H., 1969, "Elastic Plastic Deformations at Finite Strain," *ASME J. Appl. Mech.*, **36**, pp. 1–6.
- [16] Rice, M. H., McQueen, R. G., and Walsh, J. M., 1958, "Compression of Solids by Strong Shock Waves," *Solid State Phys.*, **6**, pp. 1–63.
- [17] Lee, E. H., and Liu, D. T., 1967, "Finite-Strain Elastic-Plastic Theory With Application to Plane Wave Analysis," *J. Appl. Phys.*, **38**, pp. 19–27.
- [18] Lee, E. H., and Germain, P., 1972, "Elastic-Plastic Theory at Finite Strain," *Problems of Plasticity*, A. Sawczuk, ed., Noordhoff International Publishing, pp. 117–133.
- [19] Simo, J. C., and Ortiz, M., 1985, "A Unified Approach to Finite Deformation Elastoplastic Analysis Based on the Use of Hyperelastic Constitutive Equations," *Comput. Methods Appl. Mech. Eng.*, **49**, pp. 221–245.
- [20] Weber, G., and Anand, L., 1990, "Finite Deformation Constitutive Equations and a Time Integration Procedure for Isotropic, Hyperelastic-Viscoplastic Solids," *Comput. Methods Appl. Mech. Eng.*, **79**, pp. 173–202.
- [21] Needleman, A., 1985, "On Finite Element Formulation for Large Elastic-Plastic Deformations," *Comput. Struct.*, **20**, pp. 247–257.
- [22] Green, A. E., and Naghdi, P. M., 1965, "A General Theory of an Elastic-Plastic Continuum," *Arch. Ration. Mech. Anal.*, **18**, pp. 251–281.
- [23] Marsden, J. E., and Hughes, T. J. R., 1983, *Mathematical Foundations of Elasticity*, Dover, New York.
- [24] Kratochvil, J., 1972, "Comment on Elastic Plastic Rotations," *Problems of Plasticity*, A. Sawczuk, ed., Noordhoff International Publishing, pp. 413–416.
- [25] Wang, C. C., 1970, "A New Representation Theorem for Isotropic Functions," *Arch. Ration. Mech. Anal.*, **36**, p. 198.
- [26] Milstein, F., 1980, "Review: Theoretical Elastic Behavior at Large Strains," *J. Mater. Sci.*, **15**, pp. 1071–1084.
- [27] Wang, W. M., Pozivilova, A., and Sluys, A. J., 2000, "Implicit Algorithms for Finite Deformation Viscoplasticity," *European Congress on Computational Methods in Applied Sciences and Engineering, ECCOMAS 2000*, pp. 1–15.